

IMAGE BLURRING DUE TO TURBULENT WAKES FOR AIRBORNE SYSTEMS: FLIGHT TESTS

Stanislav Gordeyev^{*a}, Nicholas De Lucca^a, Yakov Diskin^b, Eric J. Jumper^a, Matthew R. Whiteley^b

^aUniversity of Notre Dame, Notre Dame, IN, USA 46556; ^bMZA Associates Corporation., 1360 Technology Ct. Suite 200, Dayton, OH USA 45430

ABSTRACT

Image blurring and resolution degradation due to aero-optical effects around a hemispherical turret were studied experimentally in-flight using AAOL-T program at subsonic and transonic speeds. A target board consisted of spoke patterns and three-bar groups with various sizes was used to quantify the image blurring. Aero-optical effects and related image blurring were measured simultaneously using synchronized high-speed cameras. Instantaneous wavefronts were used to compute point-spread functions and modulation transfer functions. It was demonstrated that point-spread functions were mostly axisymmetric over a wide range of viewing angles and could be faithfully approximated by the Gaussian ones. Image degradation was found to be primarily dependent on the overall level of aero-optical distortions, expressed in waves, and less on spatial statistical properties of the wavefronts. Simulations of image resolution degradation using realistic aero-optical wavefront spectrum were shown to agree with experimentally-obtained results. Presented results and analysis provide means of estimating the image resolution degradation from statistics of the near-field aero-optical distortions.

Keywords: imaging, image resolution, point spread function, modulation transfer function, aero-optical effects, airborne imaging systems

1. INTRODUCTION

Aero-optical effects are optical distortions imposed on a propagating laser beam due to a varying density field around an aircraft, as the density field affects the local index-of-refraction^{1,2}. The density variations are caused by either compressibility effects at flight Mach numbers higher than 0.2 or by pressure variations. In this sense, the physical cause of aero-optical effects is different from atmospheric optical effects, which are caused by total temperature variations in the atmosphere.

It is desirable to have high-accuracy imaging systems on aircraft with a large field-of-regard. Turrets are a practical geometry for maximizing the field of regard of aircraft-mounted optical systems. They have been studied extensively in the past decade as a potential directed energy platform³. The research on turrets has focused on both experimental^{3,4,5,6} and computational^{7,8,9,10} efforts. Though the research has been focused on the use of turrets as directed energy or free-space communications platforms, the results are also applicable to their use as imaging systems.

An outgoing laser beam will get distorted by fast-moving and spatially-varying aero-optical effects, resulting in a larger than diffraction-limited laser spot and, as a consequence, a lesser intensity on a target. Likewise, an image of a distant object will be distorted by these aero-optical effects created by the turbulent flow features formed around the aircraft and, specifically, around the turret. Thus, aero-optical effects even in the absence of atmospheric optical effects will degrade the performance of an otherwise high-resolution imaging system, similar to the degradation of a beam's focusability in the far-field in the case of directed-energy or communication system.

As a precedent work, a relationship between the aero-optical environment around the turrets in flight and potential image degradation was previously explored by Whiteley and Goorskey^{R10}. In these studies, point spread functions and modulation transfer functions were computed using the wavefront data and simulations of image degradation were performed. A significant image contrast reduction at high spatial frequencies due to aero-optical effects at high transonic speeds was demonstrated.

*sgordeye@nd.edu; phone | 1-574-631-4338

This paper also examines imaging degradation, primarily image-resolution degradation due to aero-optic effects, using experimental data collected on an airborne turret system. Direct time-resolved measurements of the aero-optical distortions caused by the flow around the turret were performed in-flight at various speeds and altitudes. Independent simultaneous time-resolved measurements of image degradation due to the aero-optical effects were performed using the turret optical system as a telescope. The obtained results were used to quantify image quality in terms of commonly reported statistics for aero-optical effects so that the results of previous work can be used to predict the performance of imaging systems mounted in turrets. A companion paper¹² discusses the imaging performance of the turret as computed directly from images of a target board in-flight.

2. AERO-OPTICS OF TURRETS

As mentioned in the Introduction, turrets are often used on airborne platforms, and fluid dynamic properties of the flow around turrets and the related aero-optical effects have been studied quite intensively^{3,6,13}. Due to the bluff body shape of the turret, the incoming boundary layer rolls up into a horseshoe or necklace vortex upstream of the turret, extending in the flow direction on both sides of the turret. Due to adverse pressure gradients the flow separates on the back of the turret, forming a turbulent wake downstream of the turret. Above a freestream Mach number of $M \cong 0.55$, the flow becomes locally supersonic near the turret apex, and an unsteady shock forms. At high transonic speeds, the shock becomes strong enough to force a premature flow separation, and the motion of the separation line was shown to become coupled to the shock motion^{6,14}. These optically distorting flow features around a hemispherical turret at transonic speeds are shown in Figure 1, left.

The turret azimuthal (Az) and elevation (El) angles are often recast into viewing angle (α) and modified elevation angle (β) shown in Figure 1, right. The equations relating these angles are

$$\alpha = \cos^{-1}(\cos(Az)\cos(El)) \tag{1}$$

and

$$\beta = \tan^{-1}\left(\frac{\tan(El)}{\sin(Az)}\right). \tag{2}$$

The changed coordinate system is useful from a flow physics perspective as the viewing angle is the angle looking downstream and the modified elevation angle is the angle off the horizontal plane.

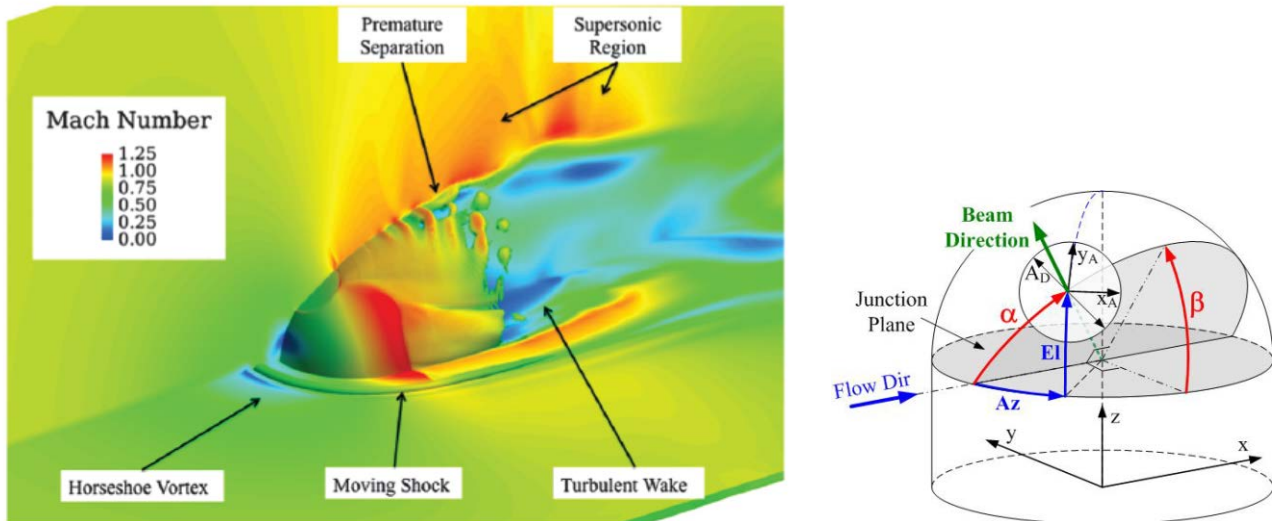


Figure 1. Left: The flow features around a turret at transonic speeds. Taken from Jelic⁸. Right: The relationship between azimuthal, elevation angles and viewing, modified elevation angles, right. Taken from Porter⁵. The transformation between these angles is given in equations 1 and 2.

The measured levels of aero-optical effects in flight, expressed in OPD_{RMS} , is shown in Figure 2. The OPD_{RMS} is a measure of the time-averaged spatial RMS of the wavefront error,

$$OPD_{RMS} = \sqrt{\overline{OPD(x,t)^2}}_x, \quad (3)$$

where the brackets denote the spatial averaging over the aperture and the overbar denotes the time average. The OPD_{RMS} gives a measure of the average deviation of the wavefront from a planar one. The OPD_{RMS} is usually provided in normalized form, $OPD_{RMS, Norm} = OPD_{RMS} \left(\frac{\rho}{\rho_{SL}} M^2 D \right)$. Here, ρ is the freestream density in flight, ρ_{SL} is the density at sea

level, M is the freestream Mach number and D is the turret diameter. This has been previously shown to collapse the data across various Mach numbers for subsonic and some transonic flows^{3,4,5,6,13}. As shown in Figure 2, the various flow features around the turret cause the OPD_{RMS} to vary with both Mach number and the viewing angle. Generally, OPD_{RMS} starts out small, near $\alpha = 80^\circ$ - 100° as the flow is attached over the turret and, at $M = 0.5$ - 0.6 , there isn't a shock present. This changes for larger Mach numbers of 0.7 - 0.8 , as the unsteady shock introduces additional density gradients with associated optical aberrations, and the OPD_{RMS} increases. At $\alpha > 100^\circ$ - 105° , the flow separates and the turbulent vortical structures in the wake introduce substantial optical distortions. The total OPD_{RMS} increases looking further back as more optical distortions got collected when the laser beam traverses through a larger region of turbulent wake. For $M = 0.7$ - 0.8 , the total optical aberrations through the wake is greater as the shock causes a premature separation and thus intensifies the wake.

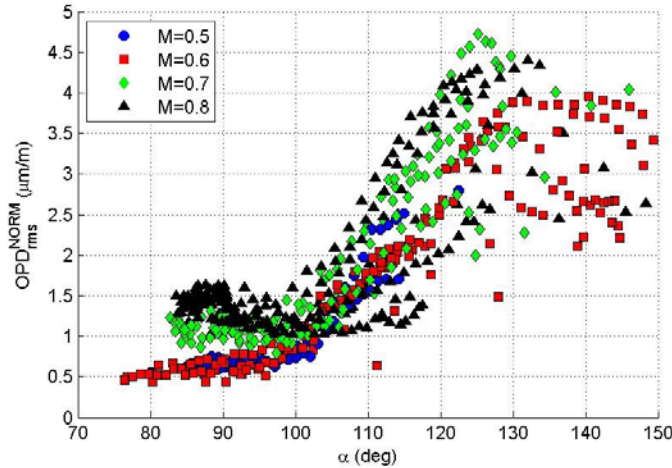


Figure 2. The normalized OPD_{RMS} versus viewing angle for a hemispherical turret as measured on the AAOL-T. Taken from Morrida⁶.

3. EXPERIMENTAL SETUP

The experiment was performed on the Airborne Aero-Optics Laboratory-Transonic (AAOL-T)¹⁵. The AAOL-T consists of two aircraft flying in closed formation with a nominal 50m separation. One of the aircraft, the source aircraft, projects a diverging 532nm laser beam onto the other laboratory aircraft shown in Figure 3. The hemispherical turret, 12-inch diameter was installed on the laboratory aircraft. The turret had a conformal window with a 4-inch diameter clear aperture. Both the incoming laser beam and the turret actively track each other using independent point-and-tracking systems, so the incoming laser beam is always directed at the turret aperture and the turret always faces the incoming laser beam; a detailed description of the tracking systems and the optical layout of the turret are provided in Jumper et al¹⁵.

To perform in-flight measurements of image degradation due to aero-optical effects, a target board, shown in Figure 4, top right, was placed on the side window of the laser aircraft, around the outgoing laser beam. A rectangular horizontal cut in the middle of the target board allowed the laser beam to be transmitted to the laboratory aircraft over a range of viewing angles. The target board consisted of a collection of patterns of three parallel bars with various lengths, widths

and orientations, similar to the ones in the USAF 1951 target board, so that image blurring could be measured to directly obtain the Modulation Transfer Function (MTF). In addition, two spoke patterns were present on the target board, providing a continuous and redundant rotation-independent means of extracting MTF.

Both the incoming laser beam, aberrated by the aero-optical distortions over the turret, and the reflected light from the target board were transmitted through the turret optical system. The received light was split between the two high-speed sensors. To collect time-resolved wavefronts, a Shack-Hartmann sensor was used. The Shack-Hartmann wavefront sensor consists of the lenslet array mounted on a high-speed Phantom v711 camera. The wavefronts were acquired at 20 kHz with the exposure time of 0.4 μ sec for 16,000 frames with a spatial resolution of 36x36 subapertures.



Figure 3. The AAOL-T laboratory aircraft with the installed turret, seen from the source aircraft during a formation flight.

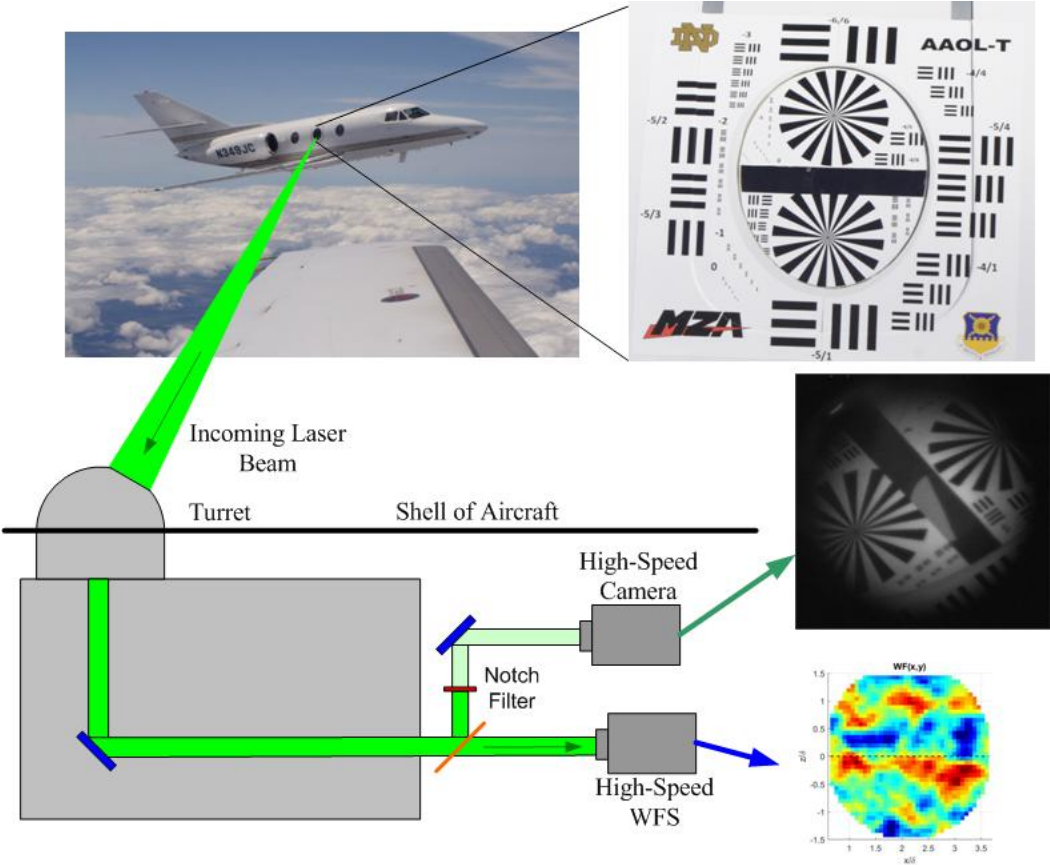


Figure 4. The schematic of the simultaneous wavefront-imaging flight experiment.

The time-resolved imaging of the scoring board, illuminated by the ambient light from the Sun, was collected using a Phantom v1611 camera. To prevent the incoming laser beam from damaging the camera, a dichroic notch filter was used. The lens for the imaging camera had an adjustable focal length from 150-500 mm with a minimum f-stop of 8. A 2x teleconverter was attached to the lens to double the effective focal length. For the actual images, the lens was set to a focal length of 300 mm, giving an effective focal length of 600 mm, and the f-stop was set to the minimum value of 8 to maximize the incoming light. The images of the scoring board were taken at 1 kHz with the exposure time of 1 msec for 5,000 frames. As the beam jitter due to mechanical motion of the turret was found to be present mostly over low frequencies below 400 Hz¹⁵, images were collected at the higher sampling speed of 1 kHz to attempt to minimize the image blurring due to beam jitter but still giving an exposure time that was large enough to collect relatively bright images.

Both cameras were triggered simultaneously to ensure their synchronization. The sampling allowed both instantaneous wavefronts and blurred images to be collected simultaneously. The flights were performed over Mach numbers between 0.5 and 0.8 and different altitudes and turret viewing angles between 80 and 150 degrees. The distance between the aircraft was measured using a differential GPS-system, capable to measuring the distance to better than 1 cm, and the distance was maintained at to be close to a nominal distance of $L = 50$ m. The flight parameters such as local flow angle of attack and static and total pressure were also acquired simultaneously with the wavefronts and imaging data, using angle-of-attack probe, installed on the laboratory aircraft.

In general, it is expected that larger aero-optical distortions will result in blurrier images. Conversely, reducing aero-optical distortions might result in image sharpening. To study this effect, a flow mitigation device, consisting of a fence, mounted upstream of the turret, was flown. This device was shown to reduce aero-optical effects caused by the unsteady shocks forming on the turret at transonic speeds¹⁶. Simultaneous wavefronts and images were also collected in flight and compared to the results without the device (the baseline).

4. DATA ANALYSIS

The OPD was computed from the Shack-Hartmann wavefront sensor images using in-house software. To measure the average aberrations over the aperture, the OPD_{RMS} was computed using equation 3. The wavefronts are simply the conjugates of OPDs, $W(x,y,t) = -OPD(x,y,t)$. Experimentally-measured wavefronts were used to compute the far-field intensity patterns¹⁷, i.e., Point-Spread Functions (PSF),

$$PSF(r_x, r_y) = \frac{\left| \int_{Aperture} \sqrt{I_0(x_A, y_A)} \exp \left[2\pi i \left\{ \frac{W(x_A, y_A)}{\lambda} - \frac{(x_A r_x + y_A r_y)}{R} \right\} \right] dx_A dy_A \right|^2}{\left| \int_{Aperture} \sqrt{I_0(x_A, y_A)} dx_A dy_A \right|^2}, (r_x, r_y) = \frac{2\pi R}{\lambda} (\theta_x, \theta_y)$$

Here I_0 is the near-field intensity, which was assumed to be a top-hat function, $R (= 2$ in) is the aperture radius and (θ_x, θ_y) are the far-field angles. The numerical integration was performed over the aperture frame of reference, (x_A, y_A) , defined in Figure 1, right. PSFs were calculated for all points collected in flight for different wavelengths between 0.2 and 1.0 microns, as PSF depends on the ratio of the aero-optical distortions and the wavelength.

For each wavefront sequence, both time-averaged Strehl Ratio, SR , and time-averaged Power-in-Bucket, PIB , were calculated. SR was defined as on-axis intensity, $SR = PSF(0,0)$, and PIB was defined as amount of energy inside the Airy's disc, relative to the energy for the diffraction-limited case. Finally, time-averaged spatial root-mean-square of wavefronts, denoted as OPD_{rms} , were calculated for all test points.

To estimate far-field on-axis Strehl ratio, the Maréchal approximation is often used,

$$SR(t) = \frac{I}{I_0} = \exp \left\{ - \left(\frac{2\pi OPD_{RMS}(t)}{\lambda} \right)^2 \right\}.$$

This approximation assumes that the spatial wavefront distribution is Gaussian. In the limit of the optical aperture being much larger than the characteristic aberrating structure size, was shown by Steinmetz¹⁸ that the Maréchal approximation holds for the time-averaged Strehl ratio as well,

$$SR = \frac{I}{I_0} = \exp\left\{-\left(\frac{2\pi OPD_{RMS}}{\lambda}\right)^2\right\}. \quad (4)$$

This approximation is called the Large Aperture Approximation (LAA). This approximation was further investigated by Porter et al¹⁹ using AAOL flight data, and it was shown that the approximation breaks down for $OPD_{RMS}/\lambda > 0.2$, with the LAA consistently underpredicting the actual SR.

Finally, Point Spread Functions were used to calculate Modulation Transfer Functions (MTF) in the standard way by performing a Fourier Transform.

5. RESULTS

Figure 5 presents the computed time-averaged Strehl ratio as a function of OPD_{rms}/λ for all Mach numbers, altitudes and viewing angles flown for both the baseline and with mitigation. Almost all points collapse along a single line, suggesting that SR mostly depends on overall level of aero-optical distortions and less on particular flow features causing aero-optical distortions. The mitigation device resulted in generally smaller values of OPD_{rms}/λ , compared to the baseline. The Large-Aperture Approximation, equation 4, is also plotted for comparison. The LAA correctly predicts SR only for small values of $OPD_{rms}/\lambda < 0.2$ and consistently under predicts Strehl ratios for larger OPD_{rms}/λ . This behavior was observed earlier²⁰ and was attributed to non-Gaussian spatial distribution of the wavefronts.

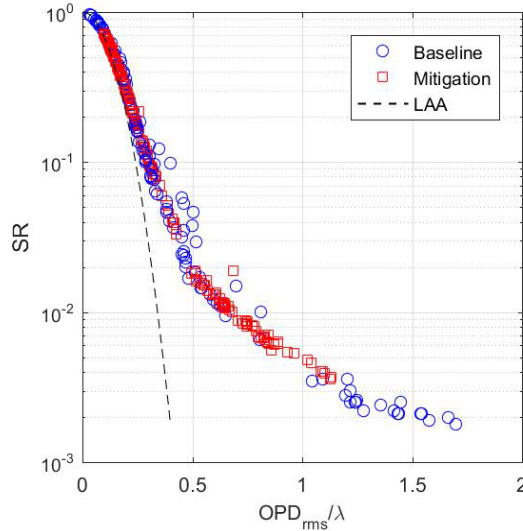


Figure 5. Time-averaged Strehl Ratio as a function of OPD_{rms}/λ for both the baseline and with the passive mitigation for different wavelengths. Large-Aperture Approximation (LAA) is indicated as a dashed line.

Figure 6 shows selected time-averaged PSFs at different viewing angles for $M = 0.8$ in the top plots and the corresponding “slices” in both r_x - and r_y - directions shown in the bottom plots. As discussed earlier, the unsteady shock forms over the turret near $\alpha = 85$ degrees. The shock spans in the vertical direction along the turret apex, so most of the wavefront spatial variations are in the direction normal to the shock. As a consequence, the PSF at this angle, shown in Figure 6, left column, has faint tails extending in the horizontal direction.

The flow separates around $\alpha = 100$ degrees and shear-layer-type structures form downstream of the separation. These structures span primarily in the vertical direction, resulted in PSF, elongated in the horizontal direction, see Figure 6,

middle column. For larger viewing angles the flow becomes fairly complex and essentially isentropic, resulted on the nearly axisymmetric PSFs, Figure 6, right column.

While some axial asymmetry was observed in PSFs, this asymmetry was found be relatively small. To compensate for the asymmetry, all PSFs were angle-averaged to create axisymmetric PSFs. The axisymmetric PSFs are plotted as dashed lines in Figure 6, bottom plots. Notice that the axisymmetric PSFs closely represent the experimental PSFs regardless of orientation.

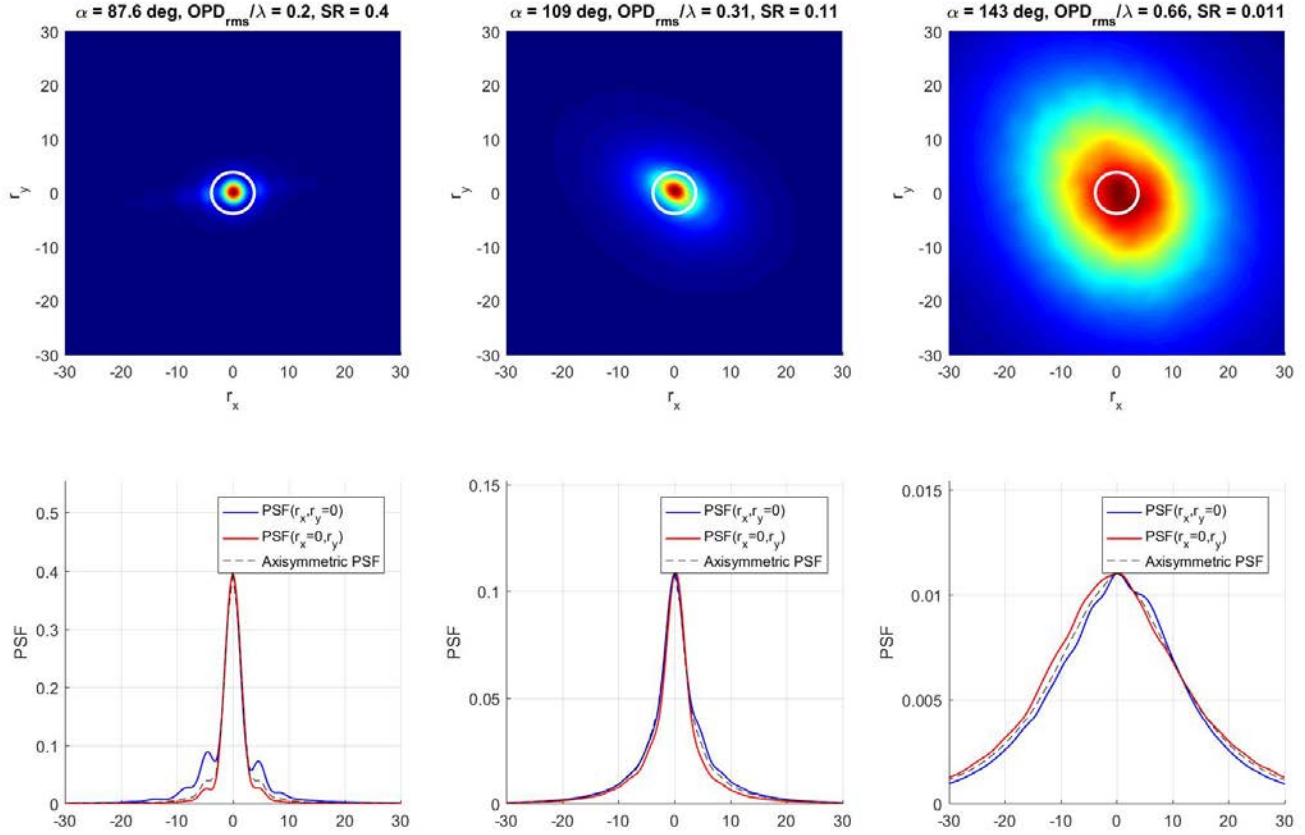


Figure 6. Time averaged PSFs, presented as two-dimensional surfaces (top plots) and as “slices” along r_x - and r_y - directions (bottom plots), computed from experimental wavefronts at selected viewing angles. Axisymmetric PSFs are plotted as dashed lines. $M = 0.8$. White circles indicate the area of Airy’s disc.

To further approximate axisymmetric PSFs, they were modelled as Gaussian surfaces,

$$PSF_{Gauss}(r) = SR \cdot \exp\left\{-\frac{r^2}{2\sigma^2}\right\}.$$

These Gaussian PSFs are uniquely defined by the time-averaged SR and σ -value. For the diffraction-limited (DL) PSF, $SR = 1$ and $\sigma_{DL} \approx 1.381$. For each experimental PSF, σ -value was computed using a least-square estimation.

To check how well the Gaussian PSF represented the real experimental PSF, axisymmetric MTFs were calculated from the experimental and Gaussian-approximated PSFs. Results for selected OPD_{rms}/λ are shown in Figure 7. Although not perfect, the Gaussian MTFs does a satisfactory job representing MTFs at low values of MTF $< 0.1 \dots 0.2$. The Gaussian

MTF is uniquely defined by the σ -value, $MTF_{Gauss}(\rho) = \exp\left\{-2\sigma^2\left(\rho\frac{\lambda L}{D}\right)^2\right\}$, where $\rho\lambda L/D$ is the normalized spatial

frequency. Thus, prescribing the σ -value is sufficient to estimate the image resolution degradation due to aero-optical effects. For instance, if MTF = 0.1 criterion is used to resolve two point sources, it is straightforward to show that $\theta_{\text{resolved}} \approx 0.93\sigma(\lambda/D)$; similarly, for MTF = 0.2 criterion, $\theta_{\text{resolved}} \approx 1.11\sigma(\lambda/D)$. For the diffraction-limited case, $\sigma_{\text{DL}} \approx 1.381$ and $\theta_{\text{resolved, DL}} \approx 1.287(\lambda/D)$, close to the standard image resolution criterion of $1.22(\lambda/D)$. Also the resolution degradation is simply the ratio between the σ -values, $\theta_{\text{resolved}}/\theta_{\text{resolved, DL}} = \sigma/\sigma_{\text{DL}}$, so defining the $\sigma/\sigma_{\text{DL}}$ -ratio is sufficient to define the image resolution degradation in the presence of aero-optical effects.

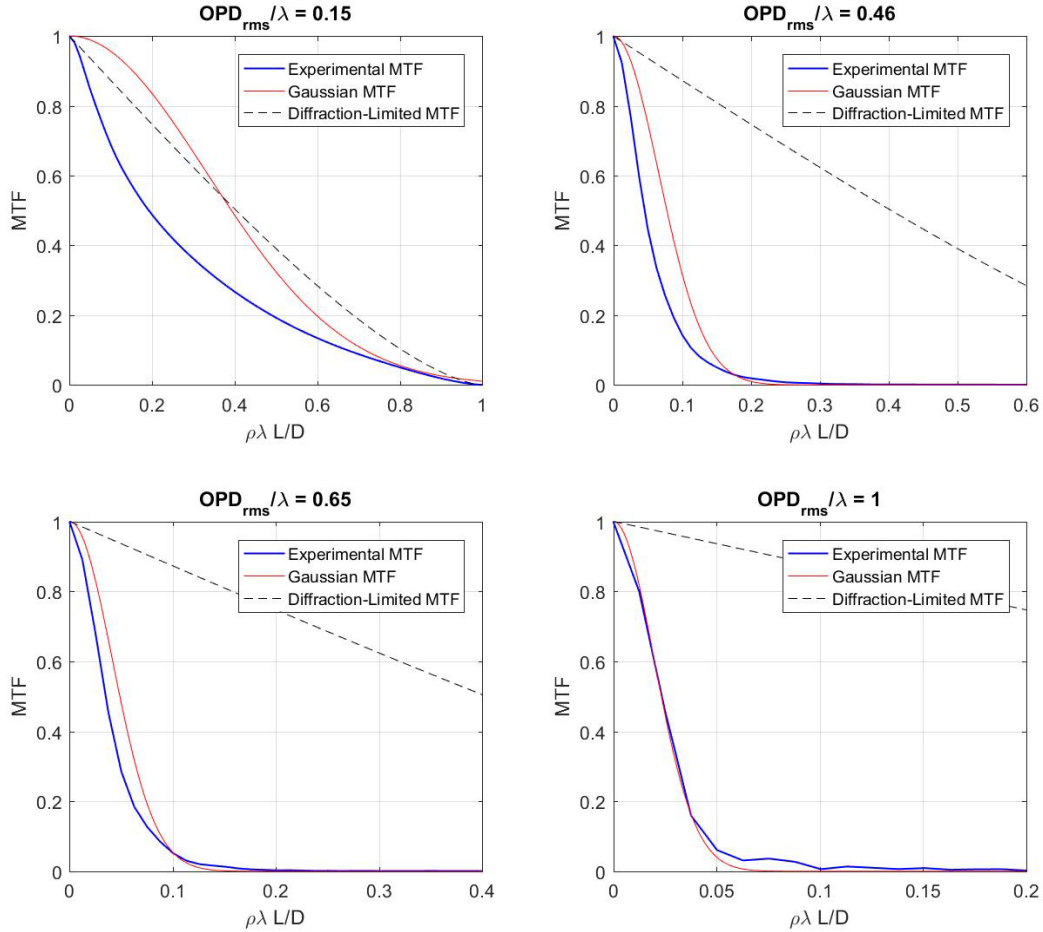


Figure 7. Experimental MTFs and the corresponding Gaussian approximations as a function of the normalized spatial frequency, $\rho\lambda L/D$, for different values of OPD_{rms}/λ . The diffraction-limited MTF is shown as a dashed line for comparison.

The ratio of $\sigma/\sigma_{\text{DL}}$ for all experimental points and wavelengths were calculated and the results are shown in Figure 8 as a function of OPD_{rms}/λ . With few exceptions, all data collapse on a single line. The ratio is close to unity for small values of $OPD_{\text{rms}}/\lambda < 0.2$, but quickly increases for larger OPD_{rms}/λ . For instance, for $OPD_{\text{rms}}/\lambda = 0.7$, $\sigma/\sigma_{\text{DL}} = 10$. It indicates the importance of including aero-optical effects to estimate the image resolution of an overall airborne system. Also, it shows that knowing OPD_{rms}/λ might be sufficient to estimate the resolution degradation of images due to aero-optical effects.

Figure 9 shows the $\sigma/\sigma_{\text{DL}}$ -ratio as a function of the time-averaged SR and PIB. Again, almost all points collapse onto single line. Moreover, over a wide range of Strehl Ratio, the $\sigma/\sigma_{\text{DL}}$ -ratios exhibit a power-law dependence on SR,

$$\sigma/\sigma_{\text{DL}} \approx 0.66 SR^{-0.57} \text{ for } 0.003 < SR < 0.48.$$

Thus, it gives a simple analytical expression relating the σ/σ_{DL} -ratio and the time-averaged SR to estimate the aero-optical effect on image resolution. Inversely, it can be used to estimate SR of the system from the measured degree of image blurriness, $\theta_{resolved}/\theta_{resolved, DL} = \sigma/\sigma_{DL}$, as $SR \approx 0.48 (\sigma/\sigma_{DL})^{-1.75}$ for $\sigma/\sigma_{DL} < 20$.

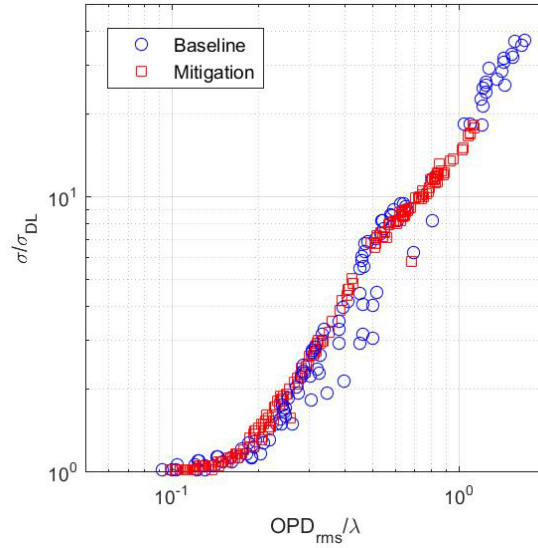


Figure 8. σ -values, normalized by the diffraction-limited value, σ_{DL} , for different OPD_{rms}/λ for the baseline and the mitigation.

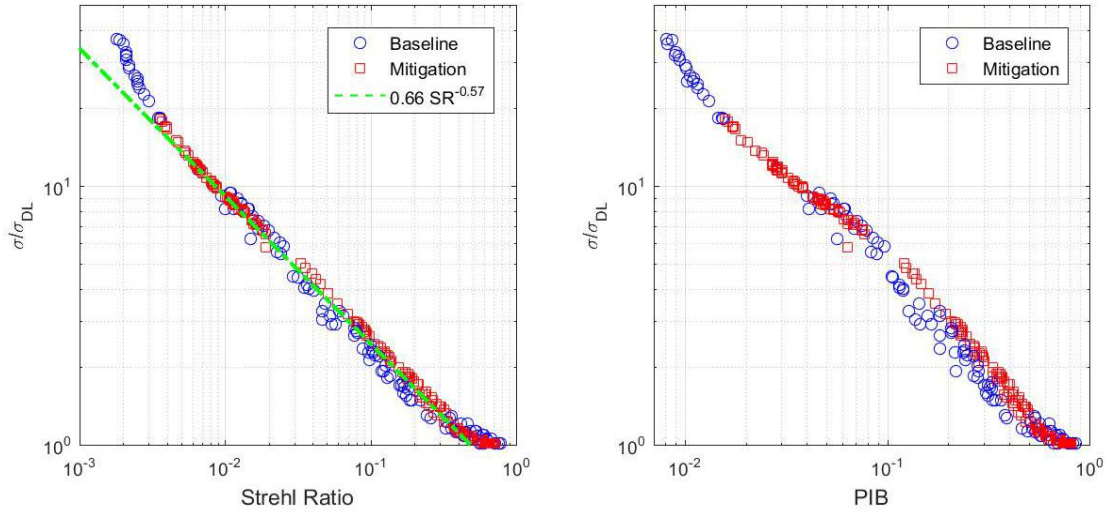


Figure 9. σ -values, normalized by the diffraction-limited value, σ_{DL} , as a function of SR (left) and PIB (right). Baseline values are indicated by blue symbols and with the mitigation are indicated by red symbols.

As the experimental results include a wide range of viewing angles with different physical sources of aero-optical distortions (shock, boundary layer, separated flow etc), the dependence of σ/σ_{DL} on Strehl ratio, presented in Figure 9, left, might be treated as a universal one. To further investigate this claim, PSF from numerically-generated axisymmetric wavefronts were calculated. The wavefronts are modelled^{20,21} by a finite sum of properly-adjusted 2-D harmonics with Gaussian-random amplitudes, A_n and B_n , and uniformly-distributed random phases, ϕ_n ,

$$W(\vec{x}) = \sum_n \sqrt{A_n^2 + B_n^2} \sqrt{\Phi(\vec{\kappa})} \exp(2\pi i \vec{\kappa} \cdot \vec{x} + \phi_n) \quad (5)$$

The 2-D wavefront spectral function, Φ , was chosen as axisymmetric, that is it is only a function of the modulus of the 2-D spatial wavenumber, $\vec{\kappa}$. Based on aero-optical studies of turbulent boundary layers²², the spectral function was chosen as

$$\Phi(\vec{\kappa}) = \frac{1}{1 + (|\vec{\kappa}|l_0)^n}.$$

The spectrum is finite at small wavenumbers and the exponent, n , defines its spectral behavior at large wavenumbers, $\Phi(\vec{\kappa}) \sim |\vec{\kappa}|^{-n}$. The length scale, l_0 , defines the dominant wavefront structure size. Aero-optical studies of the boundary layers²² and the turbulent wakes downstream of turrets²³ estimated the exponent to be $n \sim 10/3$. In contrast, the exponent of atmospheric optical turbulence is $n = 8/3$ ²⁴.

Total of 2,000 random wavefronts were generated, instantaneous piston and tip/tilt components were removed and the ensemble-averaged PSFs were calculated for a range of ensemble-averaged OPD_{rms}/λ between 0.05 and 1. Based on the wavefront analysis of experimental aero-optical distortions around the turrets⁵, the length scale was chosen to be $l_0 = D/3$. The on-axis Strehl Ratios for different OPD_{rms}/λ are presented in Figure 10 for $n = 10/3$ and $8/3$, along with the experimental ones. Although consistently underestimated, SR is better predicted with the aero-optical wavefront spectrum, $n = 10/3$, then with the atmospheric spectrum, corresponding to $n = 8/3$. This result emphasizes the fact that aero-optical distortions affect the optical system differently than the atmospheric optical effects^{25,26}.

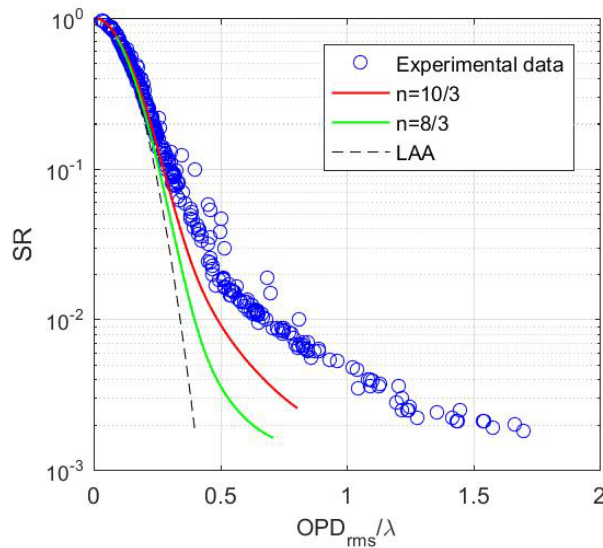


Figure 10. Ensemble-averaged Strehl ratios computed from simulated wavefronts with the aero-optical spectrum, $n = 10/3$ (red line), and with the atmospheric spectrum, $n = 8/3$ (green line). $l_0 = D/3$. Strehl ratios from experimental wavefronts are shown as symbols. Large-Aperture Approximation (LAA) is indicated as a dashed line.

The $\sigma/\sigma_{\text{DL}}$ -ratios were also calculated from the simulated PSFs and they are plotted in Figure 11 as function of SR and PIB. Assuming the aero-optical spectrum, the $\sigma/\sigma_{\text{DL}}$ -ratios agree almost perfectly with the experimentally-extracted results. On the other hand, atmospheric optical spectrum consistently under predicts the $\sigma/\sigma_{\text{DL}}$ -ratios. This implies that aero-optical effects create stronger blurring effects than the atmospheric distortions with similar Strehl ratios.

The predicted dependence of the $\sigma/\sigma_{\text{DL}}$ -ratios on OPD_{rms}/λ is shown in Figure 12. Again, the $\sigma/\sigma_{\text{DL}}$ -ratios are better predicted assuming the aero-optical spectrum than assuming the atmospheric optical spectrum.

To study the dependence of the predicted PSFs on the wavefront length scale, l_0 , additional simulations were performed with $l_0/D = 0.03$ and 1.5 and the results are presented in Figure 13. Increasing the length scale does not affect the

simulated PSFs. To understand this, recall that instantaneous piston and tip/tilt components were removed from each wavefront. This removal acts as a high-pass spatial filter^{23,25} with a cut-off value comparable with the beam diameter. So, while the large structures were present in simulated wavefronts with $l_0 = 1.5D$, most of them has been removed by subtracting piston and tip/tilt.

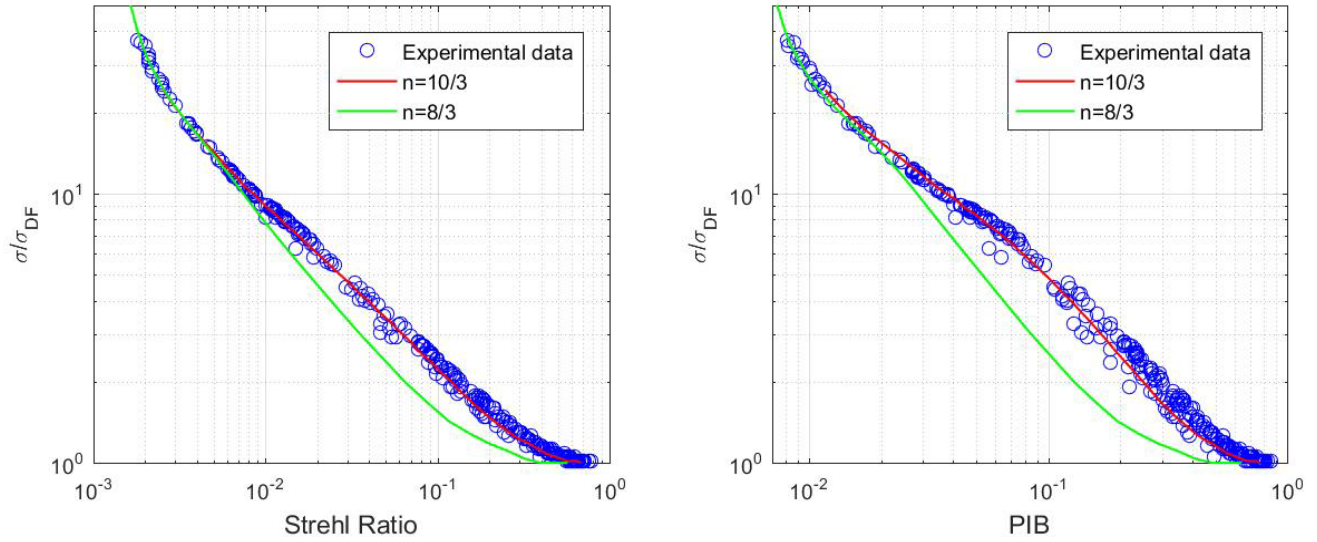


Figure 11. Predictions of σ/σ_{DL} from simulated wavefronts with the aero-optical spectrum, $n = 10/3$ (red line), and with the atmospheric spectrum, $n = 8/3$ (green line). $l_0 = D/3$. Experimental data are shown as symbols.

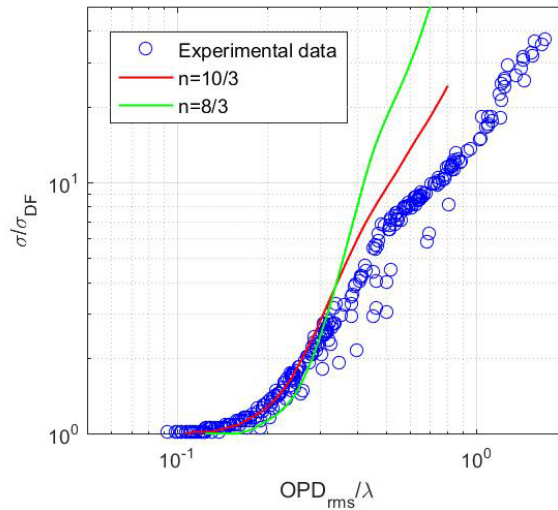


Figure 12. The predicted σ/σ_{DL} -ratios for different OPD_{rms}/λ using the aero-optical spectrum, $n = 10/3$ (red line), and using the atmospheric spectrum, $n = 8/3$ (green line). Experimental data are shown as symbols. $l_0 = D/3$.

On the other hand, if the wavefront spatial scales are small, there is almost no residual piston and tip/tilt modes present in the wavefronts. As a consequence, the wavefronts have a spatial Gaussian distribution by the means they were constructed, see equation 5. It was shown^{19,27} that if the wavefronts are Gaussian-distributed in space, the resulting averaged Strehl ratio should follow the Large-Aperture Approximation. Indeed, the predicted SR for small $l_0 = 0.03D$ follows the LAA prediction, see Figure 13, left. Also, small values of l_0 significantly under predict the σ/σ_{DL} -ratios, see Figure 13, right.

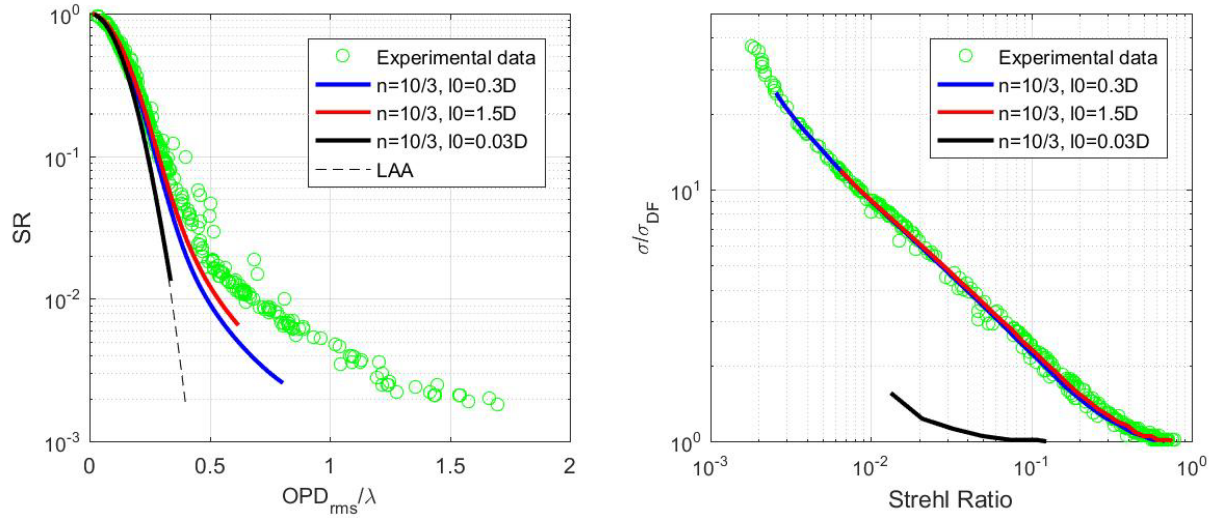


Figure 13. Left: predicted SR for different length scales, l_0 , and comparison with experimental results and LAA. Right: predicted σ/σ_{DL} -ratios for different length scales, l_0 . $n = 10/3$.

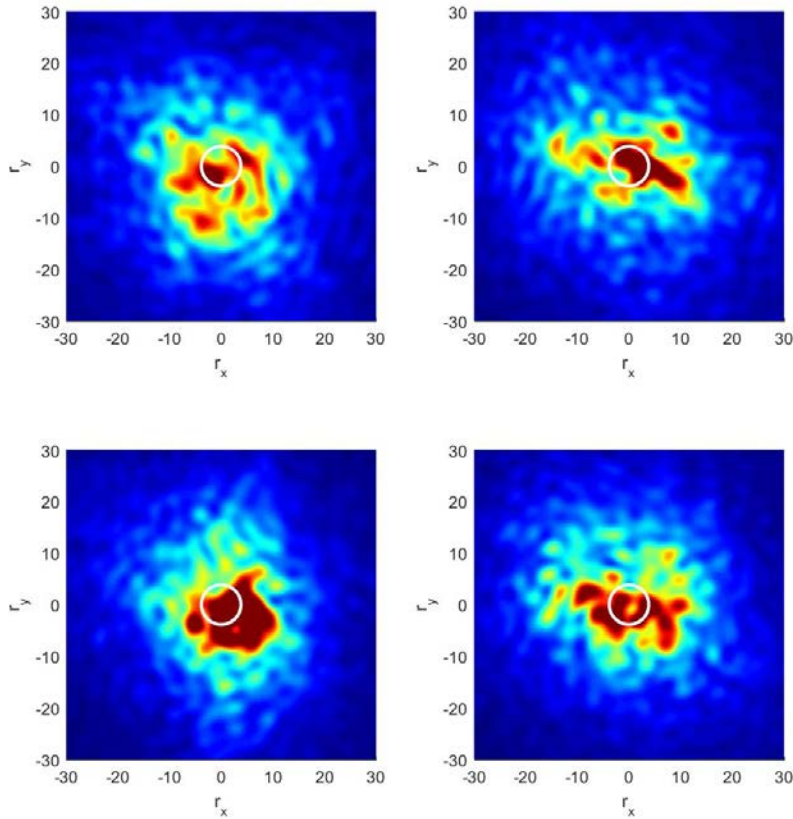


Figure 14. Instantaneous PSFs, corresponding to the time-averaged PSF shown in Figure 6, top right. A white circle in each image indicates the area of Airy's disc.

During the experiment, the images were collected at a sampling rate of 1 kHz, so the exposure time was 1 msec; the wavefronts were collected at a higher rate of 20 kHz. To investigate how the image blurring might be different for short exposure times, the instantaneous PSFs for the case corresponding to the time-averaged PSF, shown in Figure 6, top

right, were averaged over 1ms or over 20 consecutive wavefronts. Representative examples of the short-time-averaged PSF are shown in Figure 14. Clearly, the PSFs are different at different times. To compare the blurring effect for short-time-averaged images versus the time-averaged images, 50 axisymmetric short-time MTFs were computed and compared with the time-averaged axisymmetric MTF, see Figure 15. As expected, the instantaneous MTFs are either larger or smaller than the time-averaged MTF. So, the images collected over the short exposure time might be either sharper or blurrier than the time-averaged images. For instance, for $MTF = 0.2$, the normalized spatial frequency, $\rho \lambda L/D$, can be as small as 0.045 and as large as 0.08, while the time-averaged spatial frequency is about 0.06, corresponding to a relative variation of 30%.

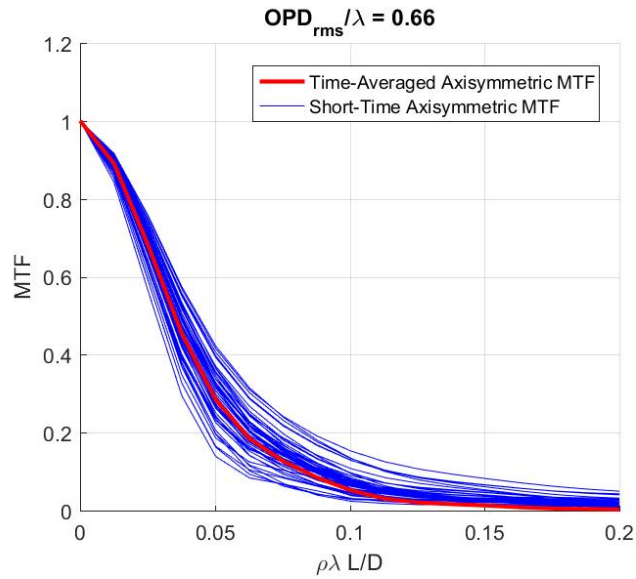


Figure 15. Short-time-averaged axisymmetric MTFs, computed using PSFs from Figure 14. The time-averaged MTF is shown as a thick red line for comparison.

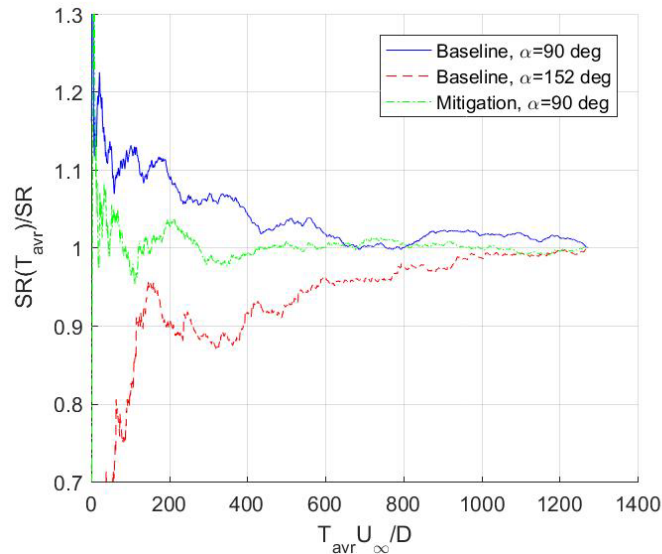


Figure 16. Convergence plot of SR-value for different averaging time intervals, T_{avr} , at selected viewing angles.

When images are collected over progressively longer exposure times, the short-time PSFs will approach the time-averaged one. To study this convergence, the on-axis Strehl Ratio, averaged over different averaging times, normalized

by the time-averaged SR, is plotted in Figure 16 for different viewing angles as a function of the averaging time, normalized by the incoming flow speed and the turret diameter. The short-time-averaged SR exhibits a large variation for short time intervals $T_{avr}U_{\infty}/D < 100$, but becomes less than 10% different from the time-averaged SR at longer time intervals $T_{avr}U_{\infty}/D > 400$. For these large averaging (or exposure) times, the time-averaged approximation, studied in this paper, should be valid.

6. CONCLUSIONS

Experimental subsonic and transonic in-flight studies of the blurring effects on images due to aero-optical distortions around hemispherical turrets were presented. Short-time-averaged images of the target board were collected in-flight using AAOL-T program, simultaneously with instantaneous aberrating wavefronts due to the turbulent flow around the turret. Using time-resolved wavefronts, point spread functions and modulation transfer functions were calculated for different transonic Mach numbers and turret viewing angles. It was demonstrated that the main parameter affecting the image resolution was the overall level of aero-optical distortions, expressed in waves, OPD_{rms}/λ . The image degradation was found to be a monotonic function of OPD_{rms}/λ and the image blurring due to aero-optical effects was estimated to become significant for $OPD_{rms}/\lambda > 0.3$. The image degradation was found to be largely independent of the spatial characteristics of the flow structures causing aero-optical aberrations. Simulations of image degradation performed using realistic aero-optical spectrum were found to faithfully predict the experimental results. When the simulations were performed using the spectrum typical of the atmospheric optical distortions, they were found to incorrectly predict the aero-optical-related image blurring. Modulation transfer functions, extracted from short time wavefronts sequences were found to vary from realization to realization. For image exposure times larger than several hundred characteristic times the image blurring was found to be converged or independent of the exposure time.

All the presented results were performed on time-resolved wavefronts, with steady wavefront and instantaneous jitter removed. Thus, effects of non-ideal optical elements and mechanically-induced turret motion were not included in this analysis. However, as the image resolution was found to be largely dependent on the overall OPD_{rms}/λ and not on specific spatial statistics of the wavefronts, it is fairly straightforward to add both steady optical distortions and the unsteady jitter effects to the presented analysis as additional OPD_{rms} components.

Another consequence of this analysis is that the direct connection of OPD_{rms} to image quality means that the imaging information alone can give an estimate of the performance of the high-energy system's performance. Also, it provides means of estimating aero-optical distortions by studying the resulting image degradation without the direct measurements involving the laser beam.

ACKNOWLEDGMENTS

This work is supported by the Joint Technology Office, Grant number FA9550-13-1-0001. The U.S. Government is authorized to reproduce and distribute reprints for governmental purposes notwithstanding any copyright notation thereon.

REFERENCES

- [1] Wang, M., Mani, A. and Gordeyev, S., "Physics and Computation of Aero-Optics," Annual Review of Fluid Mechanics, 44, 299-321 (2012).
- [2] Jumper, E.J. and Gordeyev, S., "Physics and Measurement of Aero-Optical Effects: Past and Present," Annual Review of Fluid Mechanics, 49, 419-441 (2017).
- [3] Gordeyev, S. and Jumper, E., "Fluid Dynamics and Aero-Optics of Turrets," Progress in Aerospace Sciences, 46, 388-400 (2010).
- [4] De Lucca, N., Gordeyev, S. and Jumper, E.J., "In-flight aero-optics of turrets," Optical Engineering, 52(7), 071405 (2013).

- [5] Porter, C., Gordeyev, S., Zenk, M. and Jumper, E., "Flight Measurements of the Aero-Optical Environment around a Flat-Windowed Turret," *AIAA Journal*, 51(6), 1394-1403 (2013).
- [6] Morrida, J., Gordeyev, S. and Jumper, E., "Transonic Flow Dynamics Over a Hemisphere in Flight," *AIAA Paper* 2016-1349 (2016).
- [7] Mathews, E., Wang, K., Wang, M. and Jumper, E., "LES of an Aero-Optical Turret Flow at High Reynolds Number," *AIAA* 2016-1461 (2016).
- [8] Jelic, R., Sherer, S. and Greendyke, R., "Simulation of Various Turret Configurations at Subsonic and Transonic Flight Conditions Using OVERFLOW," *Journal of Aircraft*, 50(2), 398-409 (2013).
- [9] Coirier, W.J, Porter, C., Barber, J., Stutts, J., Whiteley, M., Goorskey, D. and Drye, R., "Aero-Optical Evaluation of Notional Turrets in Subsonic, Transonic and Supersonic Regimes," *AIAA Paper* 2014-2355 (2014).
- [10] Morgan, P.E. and Visbal, M.R., "Hybrid Reynolds-Averaged Navier-Stokes/Large-Eddy Simulation Investigating Control of Flow over a Turret," *Journal of Aircraft*, 49(6), 1700-1717 (2012).
- [11] Whiteley, M. R. and Goorskey, D.J., "Imaging performance with turret aero-optical wavefront disturbances," *Optical Engineering* 52(7), 071410 (2013)
- [12] Diskin, Y., Goorskey, D., Whiteley, M.R., Drye, R., De Lucca, N., Gordeyev, S. and Jumper, E.J., "Image Blurring Due to Turbulent Wakes for Airborne Systems: Simulation and Modeling," *SPIE Optics + Photonics* 2017, 6-10 Aug, San Diego (2017).
- [13] Morrida, J., Gordeyev, S., De Lucca, N. and Jumper, E.J., "Shock-Related Effects on Aero-Optical Environment for Hemisphere-On-Cylinder Turrets at Transonic Speeds," *Applied Optics*, 56(16), 4814-4824 (2017).
- [14] Morrida, J., De Lucca, N., Gordeyev, S. and Jumper, E.J., "Simultaneous Pressure and Optical Measurements Around Hemispherical Turret in Subsonic and Transonic Flight," *AIAA-2017-3654* (2017).
- [15] Jumper, E.J., Gordeyev, S., Cavalieri, D., Rollins, P., Whiteley, M.R. and Krizo, M.J., "Airborne Aero-Optics Laboratory - Transonic (AAOL-T)," *AIAA Paper* 2015-0675 (2015).
- [16] Gordeyev, S., Burns, W.R., Jumper, E., Gogineni, S., Paul, M. and Wittich, D.J., "Aero-Optical Mitigation of Shocks Around Turrets at Transonic Speeds Using Passive Flow Control," *AIAA Paper* 2013-0717 (2013).
- [17] Klein, M.V., [Optics] 1st Edition, Wiley, New York (1970).
- [18] Steinmetz, W.J., "Second moments of optical degradation due to a thin turbulent layer," in *Aero-Optical Phenomena, Progress in Astronautics and Aeronautics*, K. G. Gilbert and L. J. Otten, Eds., 80, 78-110, AIAA, New-York (1982)
- [19] Porter, C., Gordeyev, S. and Jumper, E., "Large-Aperture Approximation for Not-So-Large Apertures," *Optical Engineering*, 52(7), 071417 (2013).
- [20] Knepp, D.L., "Multiple Phase-Screen Calculation of the Temporal Behavior of Stochastic Waves," *Proc. IEEE* 71,722 (1983).
- [21] Wittich, D.J., Gordeyev, S. and Jumper, E., "Revised Scaling of Optical Distortions Caused by Compressible, Subsonic Turbulent Boundary Layers," *AIAA Paper* 2007-4009 (2007).
- [22] Gordeyev, S., Smith, A.E., Cress, J.A. and Jumper, E.J., "Experimental studies of aero-optical properties of subsonic turbulent boundary layers," *Journal of Fluid Mechanics*, 740, 214-253 (2014).
- [23] Matthews, E. "A Numerical and Theoretical Analysis of Aero-Optics With Application to an Optical Turret," *PhD Thesis*, Notre Dame (2017).
- [24] Tatarski, V.I. [Wave Propagation in a Turbulent Medium], McGraw-Hill (1961).
- [25] Siegenthaler, J.P., Jumper, E.J. and Gordeyev, S., "Atmospheric Propagation Vs. Aero-Optics," *AIAA Paper* 2008-1076 (2008).

- [26] Gordeyev, S., Cress, J. and Jumper, E., "Far-Field Laser Intensity Drop-Outs Caused by Turbulent Boundary Layers", *Journal of Directed Energy*, 5(1), 58-75 (2013).
- [27] Ross, T.S., "Limitations and applicability of the Maréchal approximation," *Applied Optics*, 48(10), 1812–1818, (2009).